Designing Energy Dissipation Properties via Thermal Spray Coatings

M. R. W. Brake[a,b,*], A. C. Hall[a], J. D. Madison[a]

[a] *Sandia National Laboratories*[1]*, P.O. Box 5800, Albuquerque, NM 87185, USA*
[b] *William Marsh Rice University, 6100 Main St., Houston, TX 77005, USA*

Abstract

The coefficient of restitution is a measure of energy dissipation in a system across impact events. Often, the dissipative qualities of a pair of impacting components are neglected during the design phase. This research looks at the effect of applying a thin layer of metallic coating, using thermal spray technologies, to significantly alter the dissipative properties of a system. The dissipative properties are studied across multiple impacts in order to assess the effects of work hardening, the change in microstructure, and the change in surface topography. The results of the experiments indicate that any work hardening-like effects are likely attributable to the crushing of asperities, and the permanent changes in the dissipative properties of the system, as measured by the coefficient of restitution, are attributable to the microstructure formed by the thermal spray coating. Further, the microstructure appears to be robust across impact events of moderate energy levels, exhibiting negligible changes across multiple impact events.

Keywords: Thermal Spray Coatings, Impact, Coefficient of Restitution, Contact, Microstructure

1. Introduction

Energy dissipation within a system during an impact event is a velocity and material dependent property that is often associated with the plastic and viscous response of a material (Storakers et al., 1997; Ramírez et al., 1999; Ismail and Stronge, 2008; Brake, 2015). Traditionally, in order to augment the dissipative properties of a system without changing the materials, the structural design of a system (the locations of mass centers, magnitude of inertias, radii of curvatures, etc.) must be changed (Brake, 2014). An alternative approach is to change the microstructure of the

*Corresponding author; brake@rice.edu

[1] Sandia National Laboratories is a multi-mission laboratory managed and operated by Sandia Corporation, a wholly owned subsidiary of Lockheed Martin Corporations, for the U.S. Department of Energy's National Nuclear Security Administration under Contract DE-AC04-94AL85000.

contact interface (Nayeri et al., 2007); however, this can become expensive and challenging due to the necessary manufacturing processes for creating a robust microstructure that will persist across macro-scale impact events.

Thermal spray coatings (Herman et al., 2000; Smith et al., 2011; Hall et al., 2006) present a unique opportunity to change the microstructure of a surface without incurring a significant development cost. The category of thermal spray coatings encompasses several related manufacturing techniques. The commonality amongst these techniques is that particles of the size of approximately 100 nm to 1 µm are heated and sprayed onto a substrate. Depending on the specific thermal spray methodology, particle temperatures in excess of 4,000 K and particle velocities up to 1,000 m/s are achieved. Details of the manufacturing process of thermal spray coatings can be found in the review of (Pawlowski, 2008a). Presently, thermal spray coatings are used extensively to improve the wear and tribological properties of a system (Pawlowski, 2008b); however, they are known to have advantageous dissipative properties due to internal friction acting along the splat boundaries (Zolotukhin et al., 1973; Kroupa and Plesek, 2002; Patsias et al., 2006; Kroupa, 2007; Tassini et al., 2007; Torvik, 2009; Sedmák et al., 2013; Kovářík et al., 2016)

The microstructure of the coatings deposited via thermal spray methodologies is referred to as a 'splat' network. Similar to grain networks (Valiev et al., 1986; Rohrer, 2011), splat networks consist of a matrix of 'splats', each formed from the high velocity impact of a droplet of heated metal deposited on the surface via a thermal spray process. As illustrated in Fig. 1, splat networks can consist of voids, unmelted particles, and large, flattened splats. Similar to grain networks, the microstructure of splat networks can significantly affect the bulk mechanical properties of a solid (McPherson, 1989; Nakamura et al., 2000; Sevostianov et al., 2004; Trompetter et al., 2006; Sevostianov and Kachanov, 2009; Asghari et al., 2010; Valarezo and Sampath, 2011; Zivelonghi et al., 2011). For thermal spray coatings, the microstructure is dependent upon the particle conditions at impact (e.g. temperature and velocity) as well as the material properties of the particle and substrate (such as substrate roughness (Paredes et al., 2006) and moduli (Pasandideh-Fard et al., 2002)). The particle conditions are determined by the process parameters of the thermal spray, including spray pressure and composition (Wang et al., 1999; Johnston et al., 2013), particle velocity and size (Dhiman et al., 2007), and specific gas heating and acceleration source (Valarezo and Sampath, 2011) amongst other parameters (Fauchais et al., 2001; Johnston et al., 2013).

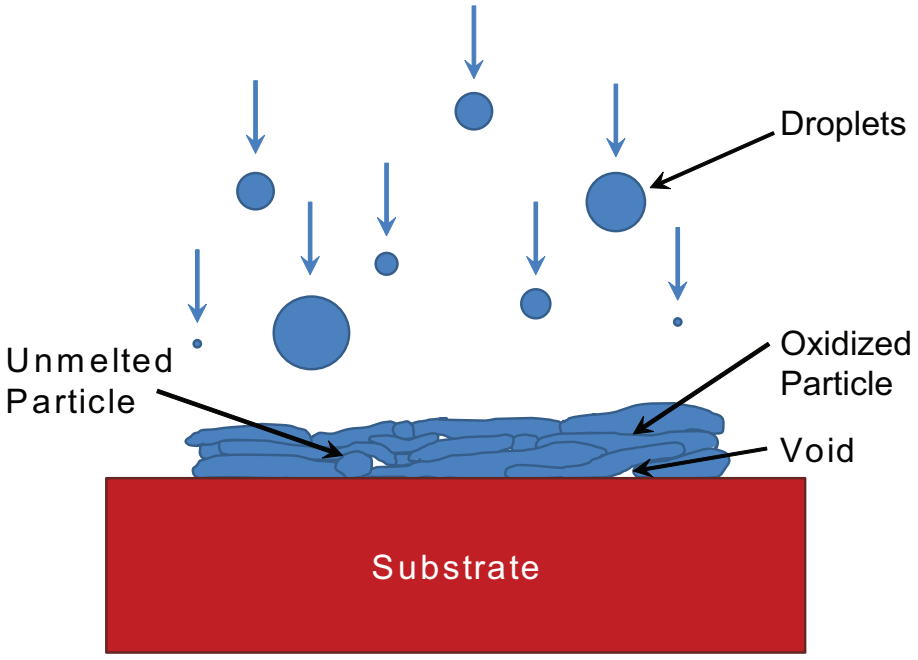

Figure 1: Illustration of the formation of a splat network from thermal spray coating methodologies.

In what follows, thermal spray coatings are investigated for engineering the dissipative behavior of a system. The thermal spray process is detailed in §2, and the dissipation measurements are reported in §3. To assess potential dissipative mechanisms, the microstructures of the impacted specimens are analyzed in §4. Finally, §5 summarizes and presents conclusions from this work.

2. Sample Preparation

Samples are fabricated using 304 stainless steel pucks that are designated into one of four conditions: control (no coating), dense coating, porous coating, and middle coating. The variations in the coating properties here are determined primarily by the thermal spray velocity, particle temperature, and flow density. The dense and porous coating conditions are intended to represent the extreme conditions that could be easily fabricated while the middle coating is an average value for the thermal spray application properties. In all cases, the coating applied to the coupons is the same: 304 stainless steel. No polishing or other conditioning is performed after the coating process[2]. The control sample, by contrast, is polished to remove all asperities larger than 100

[2]Future work would be well served to polish all specimen to the same roughness level. However, this is outside the scope of the present research.

nm. The literature on the effect of surface roughness on coefficients of restitution at a scale in which adhesive forces are negligible is somewhat limited (otherwise, see (Sahoo and Chowdhury, 2004)). The strongest conclusion observed is that surfaces with higher roughnesses exhibit a higher standard deviation in the measured responses for impacts of a sphere against a flat (Sommerfeld and Huber, 1999).

The stainless steel coatings are fabricated using a twin wire arc spray process, which is a droplet deposition coating process. A twin wire arc spray coating is applied using an arc spray torch, which brings two electrically energized feed stock wires together. When the wires cross, an arc (similar to a welding arc) forms between the wire tips, melting them. A gas stream injected behind the arc atomizes the molten feed stock material and propels it downstream. When molten droplets of the feed stock material encounter the substrate they flatten, solidify, and form a coating with the characteristic lamellar structure associated with droplet deposition.

All coatings were prepared using a Praxair/TAFA 9935 twin wire arc torch controlled using a 9910 CoArc console. The torch was outfitted with a blue nozzle and short cross nozzle positioner for all spraying. A 1.58 mm diameter 88T 300 series stainless steel wire feed stock (Praxair/TAFA) was sprayed onto 2.54 cm diameter by 3.81 cm long stainless steel substrates using dry, oil free air. The torch was mounted on an ABB-IRB 6600 six axis robot used to control standoff distance and move the torch over the substrates in a raster pattern. The raster pattern was accomplished using a 200 mm/s traverse speed, a 10 mm step size, and a 400 mm/s step speed.

The substrates were grit blasted, degreased, and cleaned before spraying. Table 1 shows the range of operating parameters used for these experiments. The 9935 torch has two primary process settings, atomizing gas flow and arc current. Wire feed rate is controlled automatically based on arc current settings such that a constant voltage and arc length is maintained across the wire tips. These parameters were chosen to produce a range of droplet velocities and droplet temperatures so as to produce a range of coating densities. In general, slower and cooler droplets are expected to produce more porous coatings than hotter and faster droplets (Fussell et al., 1994; Varacalle, Jr. et al., 1998; Wang et al., 1999; Hussary and Heberlein, 2001; Pourmousa et al., 2005; Hussary and Heberlein, 2007).

Samples were roughened using a Guyson manual grit blaster spraying Metcolite F Al_2O_3 grit (Sulzer-Metco) at 550 kPa pressure to achieve a surface roughness of approximately 14 µm Ra. After

	Hot and Fast	**Middle**	**Slow and Cool**
Standoff Distance	15 cm	30.48 cm	45.75 cm
Atomizing Air Pressure	330 kPa	234 kPa	137 kPa
Arc Current Setting	150 amps	150 amps	150 amps
Arc Voltage Setting	21 volts	21 volts	21 volts

Table 1: Torch operating condition ranges.

grit blasting, samples were rinsed with acetone and isopropyl alcohol, and dried using compressed air. Samples were thermal spray coated as soon as possible after grit blasting, with the time between grit blasting and coating never exceeding two hours. A coated sample is shown in Fig. 2.

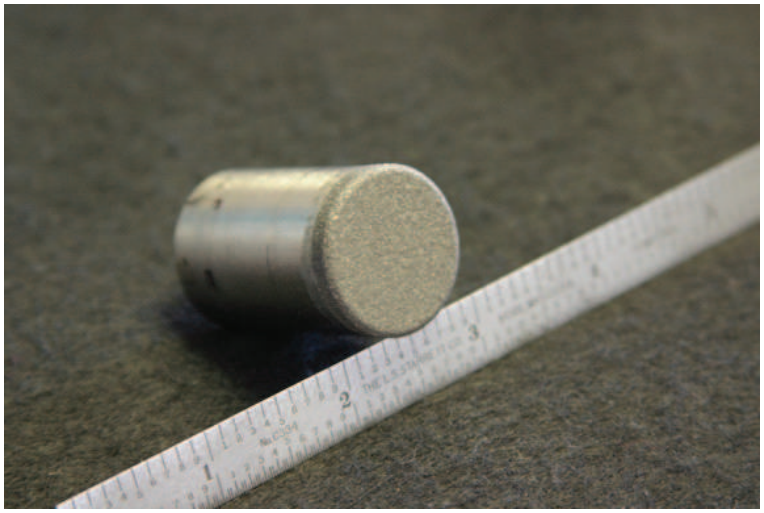

Figure 2: An arc spray coated sample.

3. Coefficient of Restitution Experiments

The coefficient of restitution is defined as a measure of the energy retained during an impact event (i.e. a coefficient of restitution of 1 corresponds to no energy loss, and a value of 0 corresponds to 100% energy loss). To measure the coefficient of restitution, a large-scale impact experiment (detailed in Section 3.1) is utilized in which a long pendulum is used to impact the test specimen at relatively low impact velocities. The large scale setup is chosen instead of a system such as a micro- or nano-indenter due to a motivation to understand the dissipative properties of the coatings in a context similar to the motivating application for this research.

3.1. Experimental Procedure

The test fixture (Baca et al., 2016; Brake et al., Under Review) developed to measure the energy dissipation properties of samples consists of a 2.1 m long pendulum with a 440c work hardened steel sphere attached to the end (Fig. 3). Samples, both coated and uncoated, are mounted on a fixed stage that is placed in the path of the 440c work hardened steel sphere of radius 1.1125 cm. One advantage of using the pendulum is increased resolution near the location of impact: even though small vertical drops are used, the pendulum allows for a long horizontal travel between the point of release and point of impact, which, in turn, enables detailed study of both elastic and plastic impacts within the same system. In order to achieve a clean release of the ball, a vacuum chuck approach is used since both magnetic and non-magnetic materials are used in related experiments. A perforated board is fixed onto the end of a vacuum line supplied by a diaphragm-type vacuum pump, and the air flow over the ball is found to impart minimal off-axis forces, which are inspected by examining the drop of the ball during each impact. A stereoscopic digital image correlation (DIC) technique (Baca et al., 2016; Brake et al., Under Review; Sutton et al., 2009) is used to measure the three-dimensional motion of the sphere during an impact event due to its high accuracy and ease of use, and a laser doppler vibrometer (LDV) is used to measure any motion that might occur in the fixture during high energy impact events.

From the coefficient of restitution equations

$$v_a^+ = \frac{m_a v_a^- + m_b v_b^- + m_b e\left(v_b^- - v_a^-\right)}{m_a + m_b} \tag{1}$$

$$v_b^+ = \frac{m_a v_a^- + m_b v_b^- + m_a e\left(v_a^- - v_b^-\right)}{m_a + m_b}, \tag{2}$$

where v^- indicates the velocity immediately before an impact, v^+ indicates the velocity immediately after an impact, m indicates the mass of an impacting body, e is the coefficient of restitution, and subscripts a and b indicate the two separate impacting bodies. For the case of $m_b \gg m_a$, with $v_b^- = 0$

$$v_a^+ \approx -e v_a^- \tag{3}$$

and

$$v_b^+ \approx 0 \tag{4}$$

for non-high speed impacts. Thus, to measure the coefficient of restitution, the velocity of the

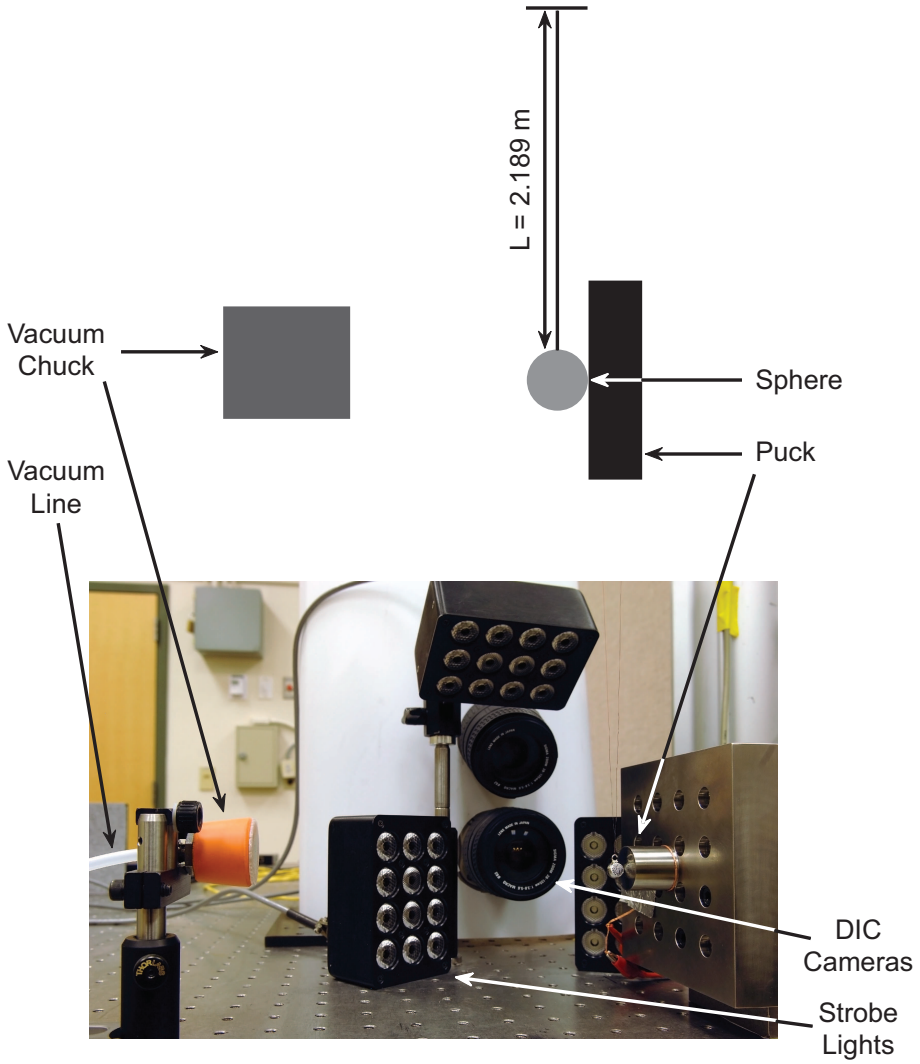

Figure 3: Schematic and photo of the experimental setup.

sphere is measured immediately before and after an impact. With the above stated assumptions, this yields that $e \approx -v_a^+/v_a^-$.

3.2. Single Impact Experiments

For the first experiment, the coefficients of restitution are measured for single impact events. After each impact, the samples are rotated 90 degrees to ensure that there are no residual effects from the previous impact measurement on the next impact measurement. Thus, each sample is used for four impacts (one on each quadrant of the coated face). The measured coefficients of restitution (Fig. 4) are compared to the control case and the predicted behavior of an un-coated sample (Brake,

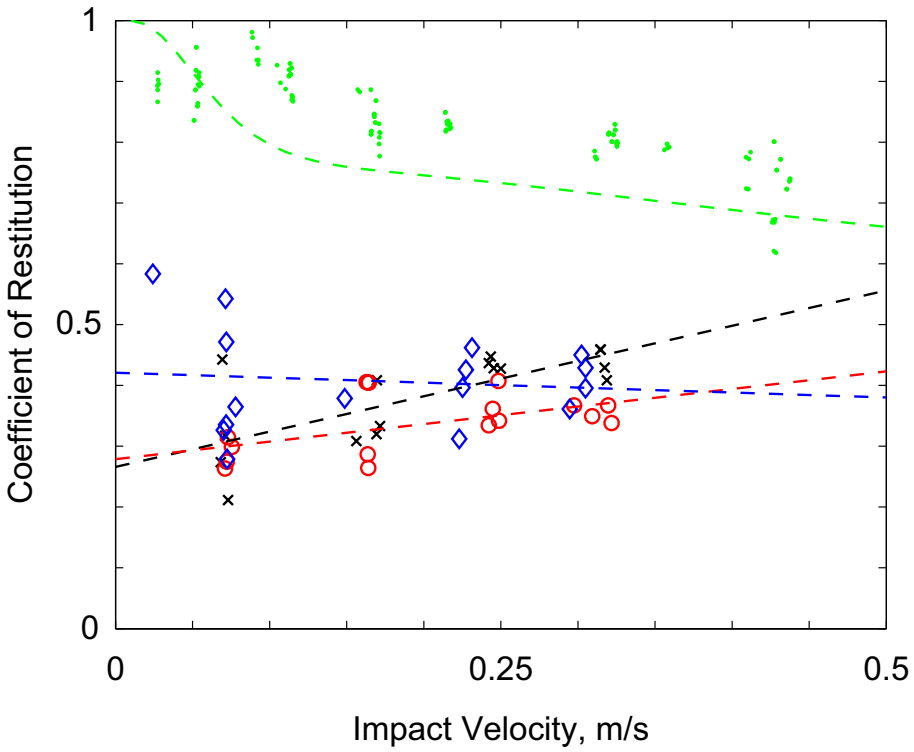

Figure 4: Measured coefficients of restitution for the un-coated control sample (·, green), the dense coating (×, black), the porous coating (∘, red), and the middle coating (⋄, blue). The linear regression lines are plotted for the three coating samples, and the prediction of (Brake, 2012) for the un-coated specimen are all plotted as dashed lines with colors corresponding to the measurements.

2015). The linear regression lines for the coated samples all show a low correlation. In all cases, the energy dissipated by the coated samples is approximately a factor of four greater than for the un-coated samples at similar impact velocities[3]. For these and all subsequent experiments, the impact energies range between 13 µJ for an impact velocity of 24 mm/s to 2.33 mJ for an impact velocity of 322 mm/s.

3.3. Multiple Impact Experiments

In order to assess the robustness of the results for the single impact experiments, a second experiment is designed in which the samples are impacted multiple times at the same location. In Figs. 5-7, the evolution of the energy dissipation properties of the coatings is shown over 20 impacts for each impact velocity on a sample. In each of the figures, the mean response of the

[3]Note that energy scales with e^2 as e is based on velocity and kinematic energy is based on the square of velocity

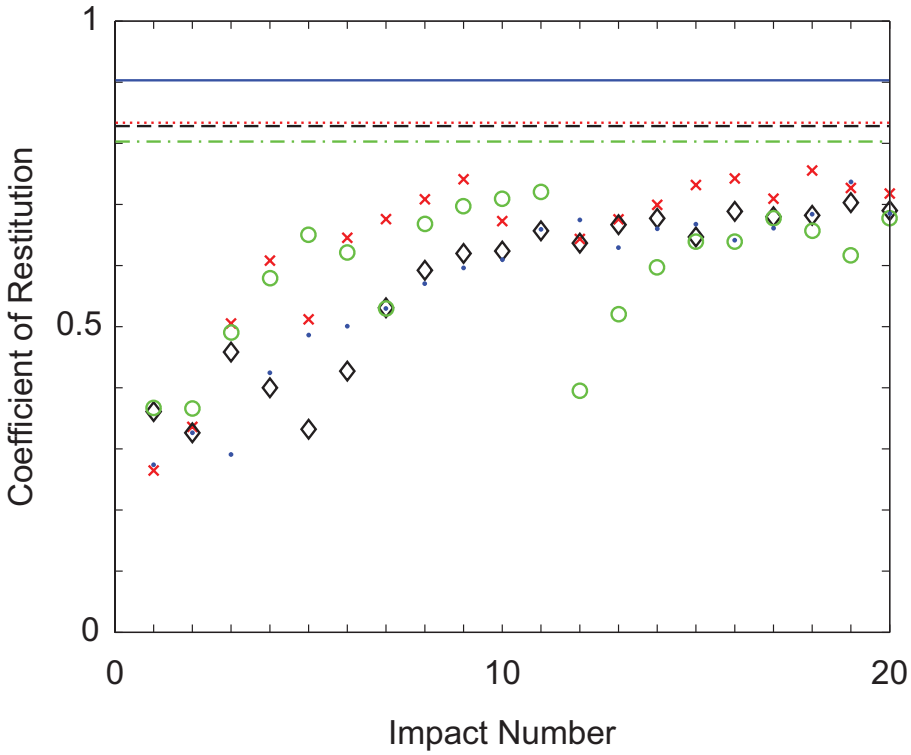

Figure 5: Measured coefficients of restitution for the porous coated sample for impacts of nominally 66 mm/s (·, blue), 148 mm/s (×, red), 225 mm/s (⋄, black), and 289 mm/s (∘, green) as a function of impact number compared against the average response of the uncoated samples at 53 mm/s (—, blue), 168 mm/s (···, red), 216 mm/s (– –, black), and 321 mm/s (– · –, green).

control sample from the single impact experiments is given as a basis for comparison.

For the porous coating, all four impact velocities studied show asymptotic behavior that converges to approximately 0.7, which is still less than the coefficient of restitution for the un-coated samples at an impact velocity of 320 mm/s (approximately 0.8). Similar trends are observed for both the middle and dense coatings as well.

3.4. Discussion of the Coefficient of Restitution Experiments

The variability in the measurements from one impact to the next is partially attributable to several sources:

- Variations in impact velocity from one impact to the next;
- Deviations in the impact location;
- Permanent change to the material/microstructure; and

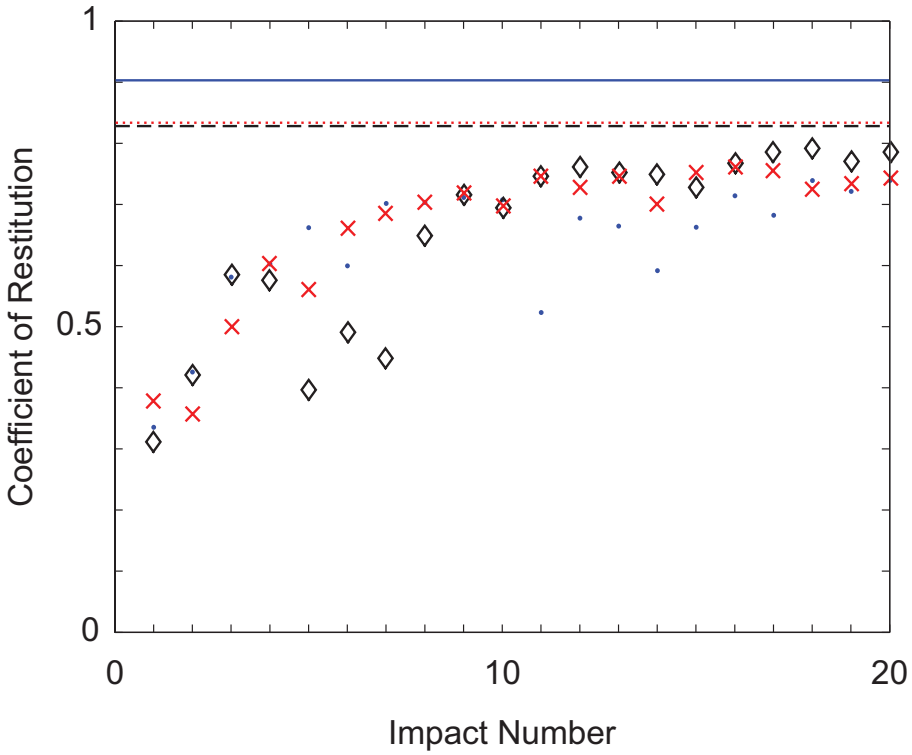

Figure 6: Measured coefficients of restitution for the middle coated sample for impacts of nominally 62 mm/s (·, blue), 139 mm/s (×, red), and 214 mm/s (⋄, black) as a function of impact number compared against the average response of the uncoated samples at 53 mm/s (—, blue), 168 mm/s (···, red), and 216 mm/s (– –, black).

- Interactions with asperities.

In order to determine if the observed dissipative behavior is primarily attributable to frictional effects at the splat boundaries within the splat network or to permanent plastic deformation of the material, each of the potential sources of variability are more closely considered.

Regarding the first source of variability, i.e. variations in impact velocity, this is quantified by the data recorded via DIC measurements. For impact velocities, standard deviations for each of the experiments on the porous samples (Fig. 5) rank 2.3 mm/s, 6.2 mm/s, 6.0 mm/s, and 10.5 mm/s in order from lowest to highest. From both the model and experiments on the control samples and coated samples (see Fig. 4), variations of these magnitudes have a negligible influence on the results compared to variations in local topography (e.g. asperity distributions, as inferred from the single impact measurements where the main difference between each impact is the local surface roughness). The standard deviations in impact velocities for all specimen are given in Table 2.

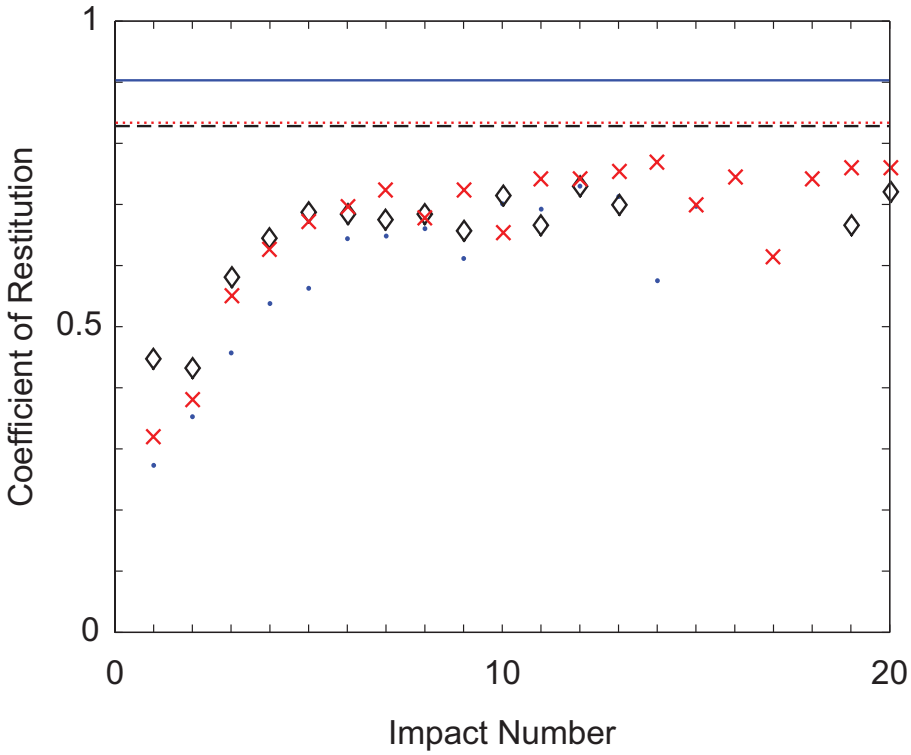

Figure 7: Measured coefficients of restitution for the dense coated sample for impacts of nominally 61 mm/s (·, blue), 142 mm/s (×, red), and 219 mm/s (⋄, black) as a function of impact number compared against the average response of the uncoated samples at 53 mm/s (—, blue), 168 mm/s (···, red), and 216 mm/s (– –, black).

For a more complete assessment of the three remaining potential sources of variability (i.e. the impact location, the effect of asperities and the permanent changes to the microstructure), the coefficient of restitution analysis is insufficient. Instead, a detailed analysis of the microstructure is needed, which is the subject of the next section.

Coating	Average (mm/s)	Standard Deviation (mm/s)
Porous	66	2.3
	148	6.2
	225	6.0
	289	10.5
Middle	62	3.2
	139	4.8
	214	4.5
Dense	61	3.2
	142	9.9
	219	7.9

Table 2: Means and standard deviations of impact velocities.

4. Metallographic Imaging

To better understand the source of dissipative mechanisms in the coated specimen, the samples were imaged in a destructive process that created a three dimensional reconstruction of the microstructure. In what follows, the metallographic imaging is detailed and the results are discussed as they pertain to the potential sources of dissipative mechanisms.

4.1. Experimental Procedure

The samples were serial-sectioned and imaged with a UES Robo-Met.3D system (Madison et al., 2008a,b, In Review) in order to measure the topological features and the splat network of the coating both in and away from the impact locations. The advantage of this serial sectioning method over other, conventional approaches (such as scanning electron miscroscopy (Deshpande et al., 2004)) is that this allows for a relatively rapid, automated, three dimensional reconstruction of the microstructure geometry over an appreciably large cross-sectional area at a resolution on the order of microns. The disadvantage is that the technique is destructive; that is, the sample is consumed as it is serial-sectioned.

Each serial-section is acquired via optical imaging. As such, full three-dimensional reconstructions are enabled by employing image-processing on the raw optical images using the image processing software FIJI. In this case, all optical images are first converted to grayscale, their histograms are autoleveled, the images are then passed through a dust and scratch filter, the noise is reduced, the processed images are cropped and aligned to remove the mount epoxy, and one final dust and scratch filter is applied prior to thresholding, resulting in optical images such as shown in Fig. 8.

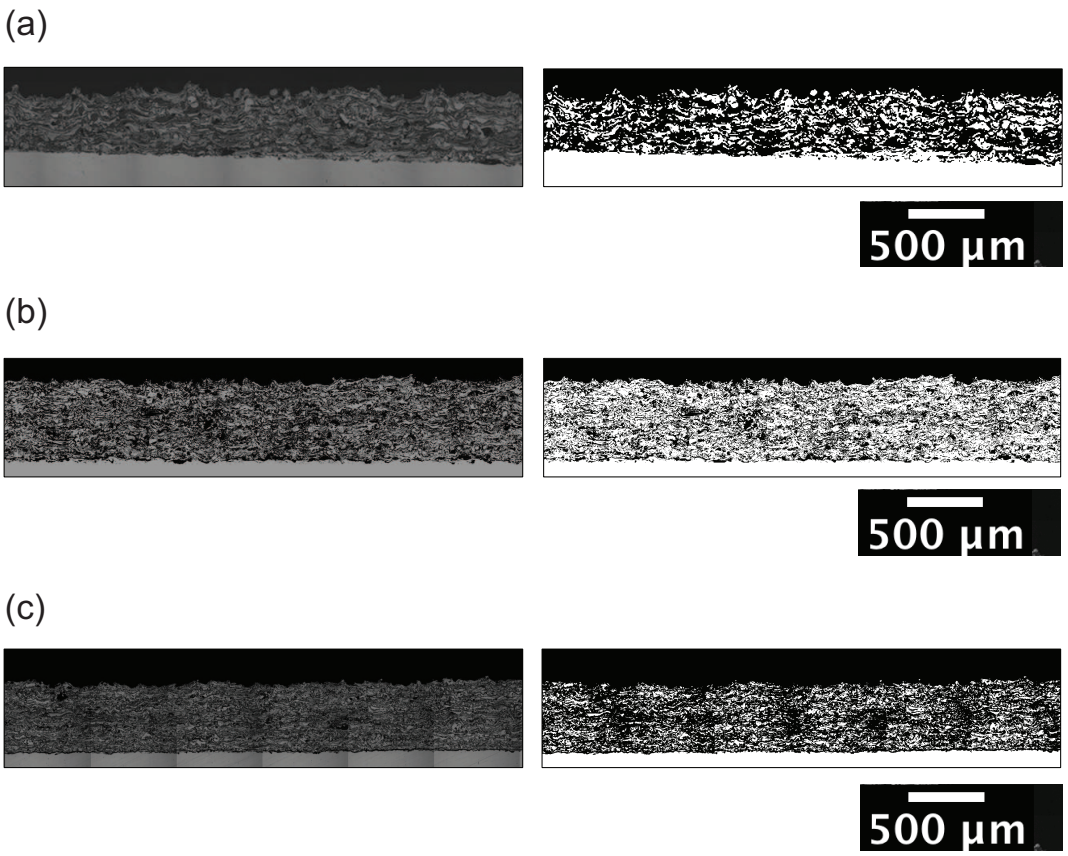

Figure 8: Optical images and processed images of (a) the porous sample, (b) the middle sample, and (c) the dense sample near the highest velocity impact location.

For each coating condition ("porous", "middle", and "dense"), the specimen tested under the highest impact velocity was selected for metallographic imaging. The samples were serial-sectioned with each serial-sectioning experiment being composed of several hundred slices having thicknesses of 7 µm or less between successive slices. This process results in a three-dimensional reconstruction of the sample's surface in addition to a visualization of the subsurface microstructure throughout the entire volume. A typical profile rendering of a three-dimensional domain of a sample is shown in Fig. 9. A hollow-tipped screw is used to indicate the impact location without disturbing the surface in the vicinity of the impact.

4.2. Metallographic Imaging Results

The three dimensional reconstructions of the samples (such as shown in Fig. 10) are used to examine the area fraction of the thermal spray coating along the length of the sample and height of

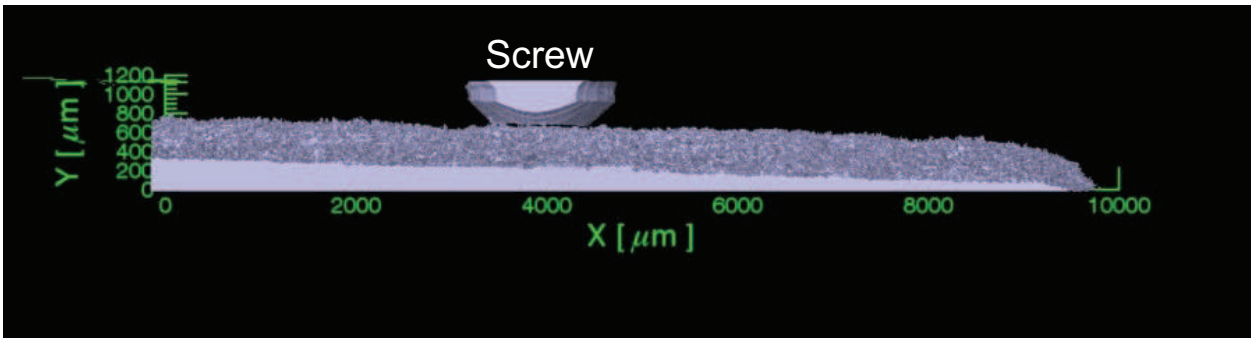

Figure 9: A typical reconstructed image of a section of the sample. The hollow-tipped screw on the top of the sample is used to indicate the impact location.

the coating. To do this, the optical images must be further processed to differentiate between solid material and voids. As shown in Fig. 11, the challenge in this process is specifying a thresholding level that includes the oxidized material (which shows up as dark grey in the optical images) but excludes pores (which show up as black). The final result (Fig. 11(c)) is then used to calculate the area fraction measurements throughout the entire reconstructed volume.

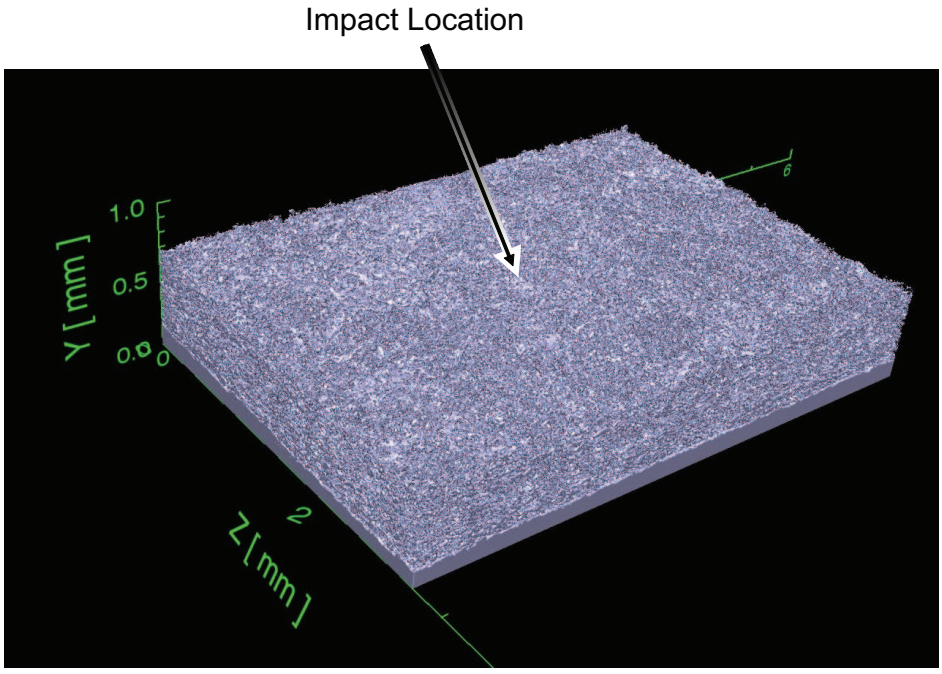

Figure 10: A typical three-dimensional reconstruction of the sample with the screw removed. Shown is the middle coating with the impact location denoted by an arrow.

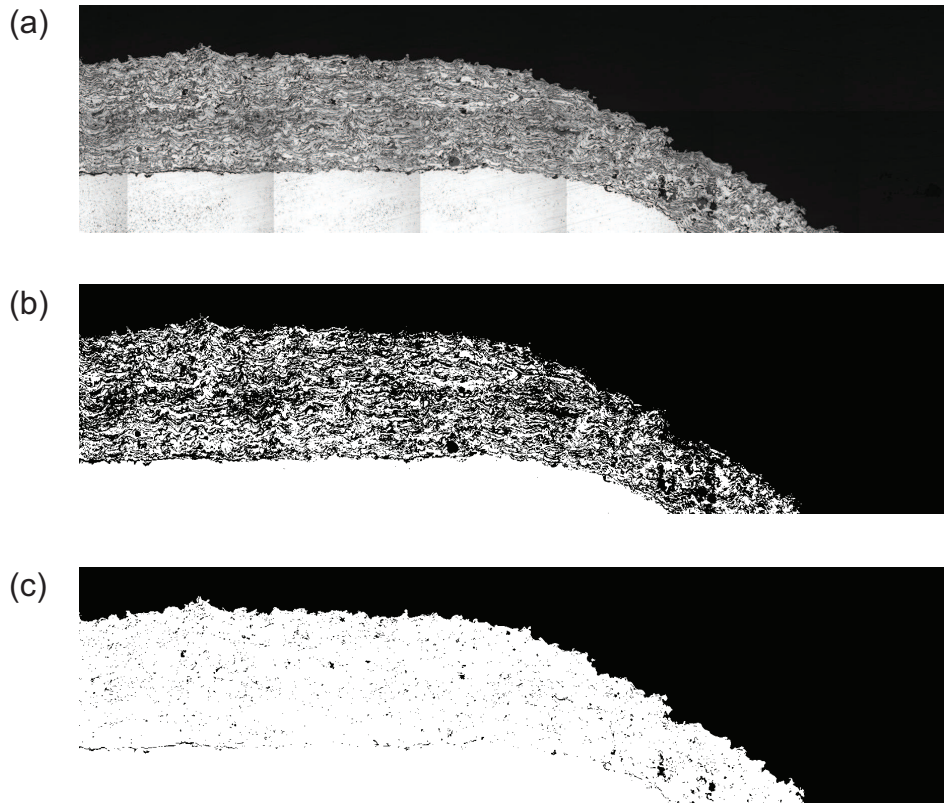

Figure 11: Processing of the image (a) from the raw serial-section, (b) to exclude pores and oxidized material, and (c) finally to exclude only pores.

The area fraction is defined as the amount of pixels, within a 2-dimensional image plane, occupied by a feature or species of interest (e.g. metal, oxide, or pores). This measure is taken across each plane in a given orthogonal direction resulting in an area fraction profile for that direction. (see Fig. 12). It is important to note that the area fraction measurements are not restricted explicitly to the spray coating themselves but rather a virtual box with dimensions equivalent to the largest dimensions of the spray coating. Thus, the box contains the spray coating but not the metallic substrate upon which the spray coating was deposited on. In this manner, the global changes in the geometry as well as the surface roughness of the spray coating are seen in the area fraction measurement. For example: an area fraction measurement taken along the entire "x" direction in Fig. 9, beginning at "0 µm" and terminating at "10000 µm" would result in a relatively constant decline followed by a rapid decrease to 0 at the end of the spray coating.

Only part of one quarter of each sample (such as shown in Fig. 2) is sectioned, so the following

naming convention is adopted: the radial axis refers to the long dimension of the sample being sectioned with radial position 0 corresponding to the center of the whole sample, the X axis refers to the short (in-plane) dimension orthogonal to the radial direction, and the vertical axis refers to the direction through the thickness of the coating.

There is no visible plastic deformation of the surface (apart from the localized damage to asperities), in the vicinity of the impact location (note the approximately straight lines in Fig. 12(b)). In the X-direction (Fig. 12(a)), the undulations correspond to imaging gradients across each tile of the montage image. However, the mean value of each agrees with what would be expected - the porous coatings have the lowest area fraction and the dense coating has the highest area fraction. No undulations are observed in the other axes as they are orthogonal to the imaging plane.

The key result in the area fraction measurement is that there is no significant or abrupt change in the area fractions aside from the global thickness of the spray coating in the radial and vertical directions. With respect to the radial axis (Fig. 12(b)), the dense coating is observed to be constant and approximately 95% area fraction throughout while the other two coatings taper off towards the edge of the samples. The linear decrease in the middle sample is a function of the overall thickness of the spray coating decreasing from the center toward the edge. Similarly, the mild decrease, followed by a near constant area fraction is an indication of the variation in thickness for the porous coating along the radial axis. In the vertical direction (Fig. 12(c)), each sample shows a markedly different starting and mean value, which is consistent with the other two directions and is to be expected. Towards the top of the samples, a decrease is observed in the area fraction that is due to the presence of asperities and a non-flat surface. If there had been an appreciable change due to the material being compressed beyond the impact locations, a notable increase in the area fraction would have been expected. However, to emphasize, no appreciable change due to the material being compressed is observed, implying that the subsurface microstructure is largely unaffected by the impacts imposed.

4.3. Discussion of the Metallographic Imaging

Returning to the three remaining potential sources of variability that were highlighted in the discussion of §3.4 (i.e. the impact location, the effect of asperities, and the permanent changes to the microstructure), the metallographic imaging is able to provide further clarity on the dissipative mechanisms. From the imaging of the microstructure of the splat networks (Fig. 13), the

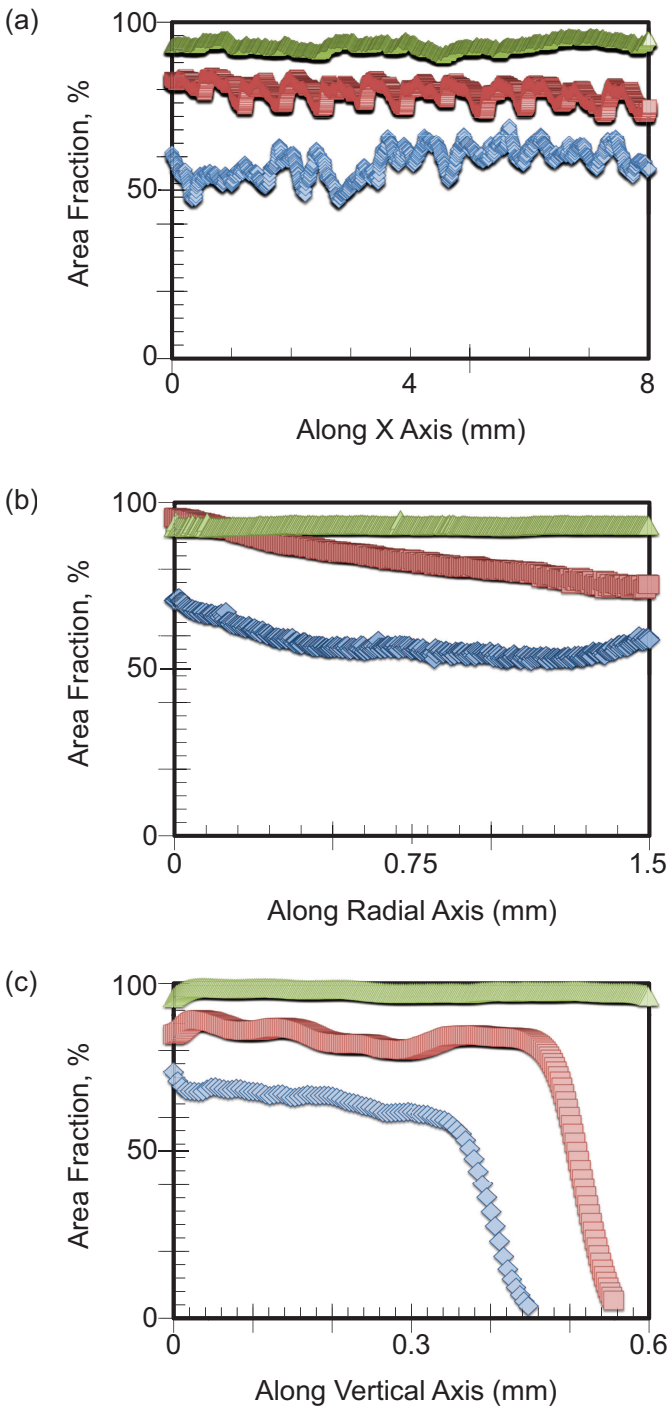

Figure 12: The area fraction of the coatings measured from the sectioning images along (a) the X axis, (b) the radial axis, and (c) the vertical axis for porous (blue diamonds), middle (red squares), and dense (green triangles) coatings.

disturbances to the microstructure (as indicated by black regions in the figure) below and near the impact locations appear to be limited to the first 30 µm of depth in most cases. Disturbances from the highest velocity impacts are observed to persist to about 90 µm of depth, and can be seen in Fig. 13 for all three coatings. From these results, there is not sufficient evidence to state definitively that the black regions correspond only to damage from impact events and not to pre-existing local topograpy. Regardless of the source of the black regions, this result indicates an upper limit on the depth of damage or microstructural irregularity in these impact experiments. Beyond 100 µm, no damage or microstructural irregularities observed in the microstructure of the specimens.

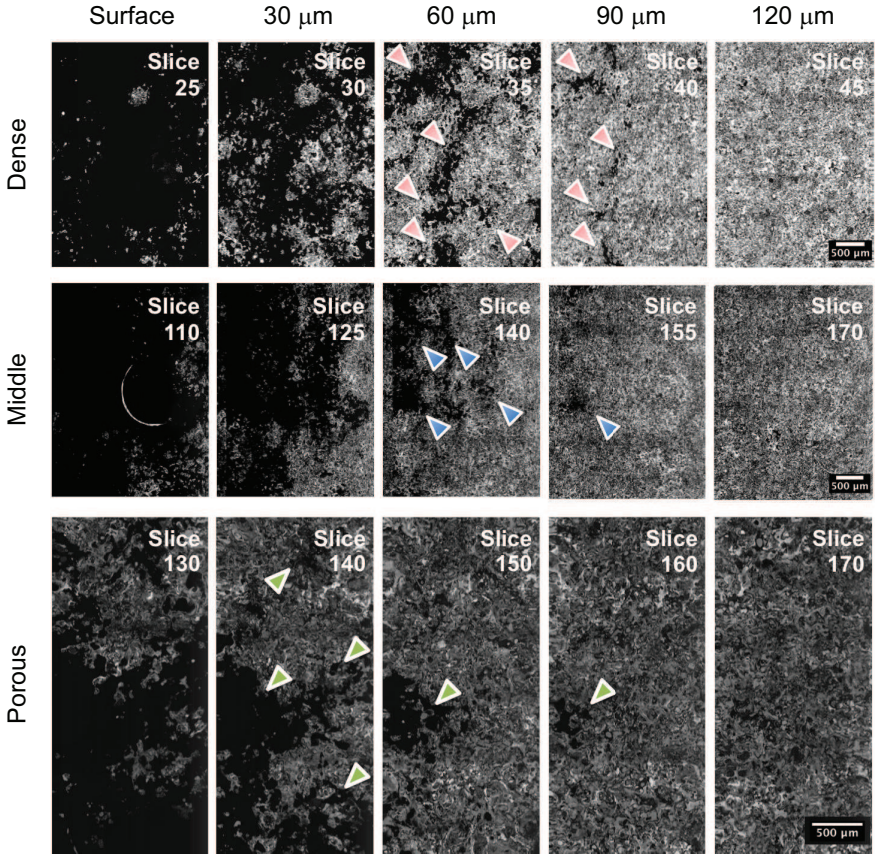

Figure 13: Optical images of the surface reconstructed from serial sectioning at five different depths: approximately 0 µm (the surface), 30 µm, 60 µm, 90 µm, and 120 µm for all three coatings. Arrows indicate features potentially due to impacts.

In the worst case scenario, all black regions could correspond to damage from impact events. If this is the case, then the arrows marked in Fig. 13 could conceivably correspond to clusters of impact locations. For the porous sample, it is observed that most impacts for the highest set of

impact velocities are within a 0.75 mm diameter circle with one outlier that is 2 mm away from the most distant impact location shown (this could be the first impact, which was made at a separate time from the 19 subsequent impacts at each impact velocity). From the model (Brake, 2015), the contact radius for the first impact at this velocity is 0.387 mm (with the contact radius increasing for subsequent impacts due to local deformations (Jackson et al., 2005)). This contact radius suggests that the impact locations overlap for each of the tests, thereby indicating that the impact location is well controlled for in these experiments[4].

Using information from both the coefficient of restitution experiments and the metallographic imaging, the first two potential sources of variation (i.e. variations in impact velocity or impact location) can be considered negligible. The only remaining two potential mechanisms to explain the observed dissipative behavior are 1) interactions with asperities and 2) changes to the microstructure. With the impact location remaining approximately constant, it is most probable that the general increase in the measured coefficient of restitution could be due to the crushing of asperities (i.e. for higher impact numbers, there are fewer remaining asperities to be crushed). Similar data are observed in both the middle (Fig. 6) and dense (Fig. 7) coatings - for the highest impact velocity tested, the impact locations all fall within the expected contact diameter, with one outlier that is likely from the initial experiment.

A second observation from Fig. 13 is that the microstructures appear to show no remnant of impacts, damage, nor initial surface roughness at depths greater than 90 µm. This indicates that there are no significant permanent changes to the subsurface microstructure, which is in agreement with the conclusions drawn from the area fraction measurements (Fig. 12). This leads to the conclusion that the dissipative behavior is due to surface effects (either the crushing of asperities or changes in the splat networks at the surface of the coating). Thus, due to the lack of an appreciable change in the subsurface microstructure coupled with the evidence of flattening of asperities from the three-dimensional reconstruction of the surface (i.e. Fig. 10), the energy dissipation mechanism for the coated samples is hypothesized to be due to frictional interactions between the splats, and the work hardening effect is hypothesized to be due to the crushing of asperities.

[4]Unfortunately, similar data is not available for the other impact velocities

5. Conclusions

The conclusions drawn in this study are that thermal spray coatings show promise for significantly reducing the coefficient of restitution for an impacting system. For the system investigated, a 50% reduction is observed in the coefficient of restitution for the initial impacts in the system, and a 20% reduction is observed in the steady-state impact behavior. Moreover, no appreciable permanent changes are observed in their microstructure for the energy levels involved in this study (apart from the crushing of asperities), which indicates that this is a valid approach for applications with repeated impacts. However, more work is needed to thoroughly assess the microstructure of the thermal spray coating and to further examine the microstructure of the control samples.

Acknowledgements

The authors would like to thank Renee Baca, Dannelle Aragon, and Phillip Reu for their assistance with the various experiments.

References

Asghari, S., Salimi, M., Salehi, M., 2010. Modeling nonlinear elastic behavior of plasma sprayed ceramics and its evolution with sintering. Materials Science and Engineering: A 527, 4241–4249.

Baca, R.N., Reu, P.L., Aragon, D.S., Brake, M.R.W., VanGoethem, D.J., Bejarano, M.V., Sumali, H., 2016. A Novel Experimental Method for Measuring Coefficients of Restitution. SAND2016-5693. Sandia National Laboratories, Albuquerque, NM.

Brake, M.R., 2012. An analytical elastic-perfectly plastic contact model. International Journal of Solids and Structures 49, 3129–3141.

Brake, M.R., 2014. The role of epistemic uncertainty of contact models in the design and optimization of mechanical systems with aleatoric uncertainty. Nonlinear Dynamics 77, 899–922.

Brake, M.R.W., 2015. An analytical elastic plastic contact model with strain hardening and frictional effects for normal and oblique impacts. International Journal of Solids and Structures 62, 104–123.

Brake, M.R.W., Reu, P.L., Aragon, D.S., Under Review. A comprehensive set of impact data for common aerospace metals. ASME Journal of Computational and Nonlinear Dynamics .

Deshpande, S., Kulkarni, A., Sampath, S., Herman, H., 2004. Application of image analysis for characterization of porosity in thermal spray coatings and correlation with small angle neutron scattering. Surface and Coatings Technology 187, 6–16.

Dhiman, R., McDonald, A.G., Chandra, S., 2007. Predicting splat morphology in a thermal spray process. Surface and Coatings Technology 201, 7789–7801.

Fauchais, P., Vardelle, A., Dussoubs, B., 2001. Quo vadis thermal spraying? Journal of Thermal Spray Technology 10, 44–66.

Fussell, P.S., Kirchner, H.O.K., Prinz, F.B., Weiss, L.E., 1994. Controlled microstructure of arc-sprayed metal shells. Journal of Thermal Spray Technology 3, 148–161.

Hall, A.C., Cook, D.J., Neiser, R.A., Roemer, T.J., Hirschfeld, D.A., 2006. The effect of a simple annealing heat treatment on the mechanical properties of cold-sprayed aluminum. Journal of Thermal Spray Technology 15, 233–238.

Herman, H., Sampath, S., McCune, R., 2000. Thermal spray: Current status and future trends. MRS Bulletin 25, 17–25.

Hussary, N.A., Heberlein, J.V.R., 2001. Atomization and particle-jet interactions in the wire-arc spraying process. Journal of Thermal Spray Technology 10, 604–610.

Hussary, N.A., Heberlein, J.V.R., 2007. Effect of system parameters on metal breakup and particle formation in the wire arc spray process. Journal of Thermal Spray Technology 16, 140–152.

Ismail, K.A., Stronge, W.J., 2008. Impact of viscoplastic bodies: Dissipation and restitution. ASME Journal of Applied Mechanics 75, 061011–1–5.

Jackson, R.L., Chusoipin, I., Green, I., 2005. A finite element study of the residual stress and deformation in hemispherical contacts. ASME Journal of Tribology 127, 484–493.

Johnston, A.L., Hall, A.C., McCloskey, J.F., 2013. Effect of process inputs on coating properties in the twin-wire arc zinc process. Journal of Thermal Spray Technology 22, 856–863.

Kovářík, O., Haušild, P., J.‘Čapek, Medřický, J., Siegl, J., Mušálek, R., Pala, Z., Curry, N., Björklund, S., 2016. Resonance bending fatigue testing wiwth simultaneous damping measurement and its application on layered coatings. International Journal of Fatigue 82, 300–309.

Kroupa, F., 2007. Nonlinear behavior in compression and tension of thermally sprayed ceramic coatings. Journal of Thermal Spray Technology 16, 84–95.

Kroupa, F., Plesek, J., 2002. Nonlinear elastic behavior in compression of thermally sprayed materials. Materials Science and Engineering: A 328, 1–7.

Madison, J., Poulter, G., Huffman, E., In Review. Acquisition of real-time operation analytics for an automated serial-sectioning system. Integrating Materials and Manufacturing Innovation .

Madison, J., Spowart, J.E., Rowenhorst, D.J., Fiedler, J., Pollock, T.M., 2008a. Characterization of three-dimensional dendritic structures in nickel-base single crystals for investigation of defect formation, in: Superalloys, Champion, PA.

Madison, J., Spowart, J.E., Rowenhorst, D.J., Pollock, T.M., 2008b. The three-dimensional reconstruction of the dendritic structure at the solid-liquid interface of a Ni-based single crystal. JOM 60, 26–30.

McPherson, R., 1989. A review of microstructure and properties of plasma sprayed ceramic coatings. Surface and Coatings Technology 39, 173–181.

Nakamura, T., Qian, G., Berndt, C.C., 2000. Effects of pores on mechanical properties of plasma-sprayed ceramic coatings. Journal of the American Ceramic Society 83, 578–584.

Nayeri, R.D., Masri, S.F., Caffrey, J.P., 2007. Studies of the performance of multi-unit impact damers under stochastic excitation. ASME Journal of Vibration and Acoustics 129, 239–251.

Paredes, R.S.C., Amico, S.C., d'Oliveira, A.S.C.M., 2006. The effect of roughness and pre-heating of the substrate on the morphology of aluminium coatings deposited by thermal spraying. Surface and Coatings Technology 200, 3049–3055.

Pasandideh-Fard, M., Pershin, V., Chandra, S., Mostaghimi, J., 2002. Splat shapes in a thermal spray coating process: Simulations and experiments. Journal of Thermal Spray Technology 11, 206–217.

Patsias, S., Tassini, N., Lambrinou, K., 2006. Ceramic coatings: Effect of deposition method on damping and modulus of elasticity for yttria-sabilized zirconia. Materials Science and Engineering: A 442, 504–508.

Pawlowski, L., 2008a. Finely grained nanometric and submicrometric coatings by thermal spraying: A review. Surface and Coatings Technology 202, 4318–4328.

Pawlowski, L., 2008b. The Science and Engineering of Thermal Spray Coatings. John Wiley and Sons, Ltd.

Pourmousa, A., Mostahgimi, J., Abedini, A., Chandra, S., 2005. Particle size distribution in a wire arc spraying system. Journal of Thermal Spray Technology 14, 502–510.

Ramírez, R., Pöschel, T., Brilliantov, N.V., Schwager, T., 1999. Coefficient of restitution of colliding viscoelastic spheres. Physical Review E 60, 4465–4472.

Rohrer, G.S., 2011. Measuring and interpreting the structure of grain-boundary networks. Journal of the American Ceramic Society 94, 633–646.

Sahoo, P., Chowdhury, S.K.R., 2004. Normal impact of rough surfaces in presence of adhesion. Tribology International 37, 667–675.

Sedmák, P., Seiner, H., Sedlák, P., Landa, M., Mušálek, R., Matějíček, J., 2013. Application of resonant ultrasound spectroscopy to determine elastic constants of plasma-sprayed coatings with high internal friction. Surface and Coatings Technology 232, 747–757.

Sevostianov, I., Kachanov, M., 2009. Elastic and conductive properties of plasma-sprayed ceramic coatings in relation to their microstructure: An overview. Journal of Thermal Spray Technology 18, 822–834.

Sevostianov, I., Kachanov, M., Ruud, J., Lorraine, P., Dubois, M., 2004. Quantitative characterization of microstructures of plasma-sprayed coatings and their conductive and elastic properties. Materials Science and Engineering: A 386, 164–174.

Smith, M.F., Hall, A.C., Fleetwood, J.D., Meyer, P., 2011. Very low pressure plasma spray: A review of an emerging technology in the thermal spray community. Coatings 1, 117–132.

Sommerfeld, M., Huber, N., 1999. Experimental analysis and modelling of particle-wall collisions. International Journal of Multiphase Flow 25, 1457–1489.

Storakers, B., Biwa, S., Larsson, P.L., 1997. Similarity analysis of inelastic contact. International Journal of Solids and Structures 34, 3061–3083.

Sutton, M.A., Orteu, J.J., Schreier, H.W., 2009. Image Correlation for Shape, Motion and Deformation Measurements: Basic Concepts, Theory and Applications. Springer, New York.

Tassini, N., Lambrinou, K., Mircea, I., Bartsch, M., Patsias, S., Van der Biest, O., 2007. Study of the amplitude-dependent mechanical behavior of yttria-stabilised zirconia thermal barrier coatings. Journal of the European Ceramic Society 27, 1487–1491.

Torvik, P.J., 2009. Determination of mechanical properties of non-linear coatings from measurements with coated beams. International Journal of Solids and Structures 46, 1066–1077.

Trompetter, W., Hyland, M., McGrouther, D., Munroe, P., Markwitz, A., 2006. Effect of substrate hardness on splat morphology in high-velocity thermal spray coatings. Journal of Thermal Spray Technology 15, 663–669.

Valarezo, A., Sampath, S., 2011. An integrated assessment of process-microstructure-property relationships for thermal sprayed NiCr coatings. Journal of Thermal Spray Technology 20, 1244–1258.

Valiev, R.Z., Gertsman, V.Y., Kaibyshev, O.A., 1986. Grain-boundary structure and properties under external influences. Physica Status Solidi A-Applied Research 97, 11–56.

Varacalle, Jr., D.J., Zeek, D.P., Zanchuck, V., Sampson, E., Couch, K.W., Benson, D., Cox, G.S., 1998. Experimental studies of twin-wire electric arc sprayed zinc/aluminum alloy coatings. Journal of Thermal Spray Technology 7, 513–520.

Wang, X., Heberlein, J., Pfender, E., Gerberich, W., 1999. Effect of nozzle configuration, gas pressure, and gas type on coating properties in wire arc spray. Journal of Thermal Spray Technology 8, 565–575.

Zivelonghi, A., Brendel, A., Lindig, S., Nawka, S., Kieback, B., You, J.H., 2011. Microstructure-based analysis of thermal and mechanical behaviors of W/CuCrZr composites and porous W coating. Journal of Nuclear Materials 417, 536–539.

Zolotukhin, I.V., Akinin, K.G., Abramov, V.V., Netusov, Y.K., Skorobogatov, V.S., Svedomtsev, N.V., 1973. The damping and elastic characterisitics of plasma-sprayed coatings of tungsten, nicrhome, zirconia, and chromium-nickel spinels. Strength of Materials 5, 1120–1123.